Analytical Methods

ROYAL SOCIETY OF CHEMISTRY

COMMUNICATION

Cite this: *Anal. Methods*, 2026, **18**, 3928

Received 8th February 2026
Accepted 3rd May 2026

DOI: 10.1039/d6ay00236f

rsc.li/methods

PolyA-tail-mediated assembly of a gold nanoparticle-based turn-on fluorescent aptasensor for ultrasensitive detection of perfluorooctanoic acid

Zhuo-Ying Li,[ab] Li-Xia Yan,[c] Xu Zhao,[ab] Hua Lin,[d] Li-Jian Chen *[ab] and Xiu-Ping Yan[ab]

A turn-on fluorescent aptasensor for PFOA is developed using a polyA-tailed aptamer anchored on gold nanoparticles and a fluorescently labeled cDNA. The displacement of cDNA by PFOA restores fluorescence, enabling ultrasensitive detection with a 1.3 nmol L^{-1} limit, demonstrated by satisfactory recovery in spiked fish samples.

Perfluorooctanoic acid (PFOA), a representative and highly persistent perfluoroalkyl substance, has been globally regulated due to its confirmed risks to human health and ecosystems.[1,2] Stringent limits, such as the U.S. Environmental Protection Agency's health advisory of 4 ng L^{-1} for drinking water, demand analytical methods capable of ultra-trace-level detection. While conventional methods like liquid chromatography-tandem mass spectrometry are reliable, their reliance on sophisticated equipment and complex sample pretreatment limits their utility for rapid, on-site screening.[3–6] Alternative sensors based on nanomaterials such as metal–organic frameworks often rely on non-specific interactions (*e.g.*, hydrophobicity, electrostatic interactions, and F–F affinity), which may suffer from compromised selectivity in complex matrices.[7–10] Additionally, the multi-step synthesis and modification required for many functional materials limit their practical applicability.[11–13]

Aptamer-based biosensors offer a promising path toward specific and deployable detection.[14–17] In particular, coupling aptamers with gold nanoparticles (AuNPs) in a fluorescence resonance energy transfer (FRET) configuration provides a sensitive and homogeneous assay format.[18–20] However, conventional strategies for immobilizing aptamers onto AuNPs present some limitations. Thiol-based conjugation, while widely used, often requires lengthy salt-aging procedures (typically >24 h) and careful pre-reduction of disulfide bonds. Alternatively, direct physical adsorption of unmodified aptamers onto AuNPs offers simplicity but lacks control over surface density and orientation, and the weak non-covalent binding leads to poor colloidal stability under physiological salt conditions and susceptibility to displacement by competing molecules in complex matrices. These challenges highlight the need for an immobilization strategy that combines operational simplicity with robust, well-oriented aptamer attachment.[21–25]

The polyA-tail-mediated approach avoids the need for thiol modification or complex conjugation chemistry, and can be completed within approximately 3 h through a simple freeze-assisted assembly process. The polyA tail serves as a dedicated anchoring block that adsorbs preferentially onto the gold surface, allowing the aptamer sequence to extend outward in a well-defined upright orientation favorable for target recognition and cDNA hybridization.[26–29] Herein, a robust and simple turn-on aptasensor was developed for the ultrasensitive detection of PFOA. The sensing probe is constructed by immobilizing an aptamer,[30] modified with a continuous adenine sequence (polyA tail), onto gold nanoparticle (AuNP) surfaces. This is followed by hybridization with a short, fluorophore (FAM)-labeled complementary DNA (cDNA) strand (Table S1). In this probe, the FAM dye is brought into close proximity to the AuNP surface, resulting in efficient initial fluorescence quenching *via* FRET. PFOA triggers a conformational change in the aptamer, displacing the cDNA and restoring fluorescence (Fig. 1). The proposed sensor demonstrates excellent sensitivity, high selectivity, and successful application in spiked fish meat samples, showcasing potential for environmental and food safety analysis.

AuNPs were synthesized *via* the classical citrate reduction method. The as-prepared AuNPs are spherical, well-dispersed, and exhibit uniform size with an average diameter of 13 ± 2 nm (Fig. 2A). The AuNPs display a typical surface plasmon resonance absorption peak in the UV-vis spectrum with a characteristic absorption peak at 520 nm (Fig. S1). Conjugation of PFOA aptamers onto AuNPs is followed by cryogenic freezing. As

[a]*Institute of Analytical Food Safety, School of Food Science and Technology, Jiangnan University, Wuxi 214122, China*

[b]*Key Laboratory of Screening, Prevention, and Control of Food Safety Risks, State Administration for Market Regulation, Wuxi 214122, China*

[c]*Analysis and Testing Center, Jiangnan University, Wuxi 214122, China. E-mail: chenlijian123@jiangnan.edu.cn*

[d]*Food Safety Detection Key Laboratory of Sichuan Province, Chengdu 610041, China*

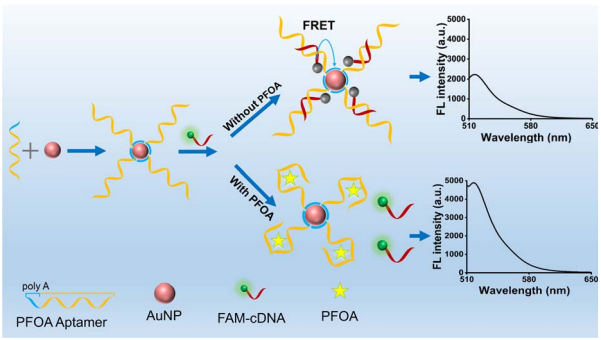

Fig. 1 Schematic illustration of the AuNP based FRET aptasensor for the detection of PFOA.

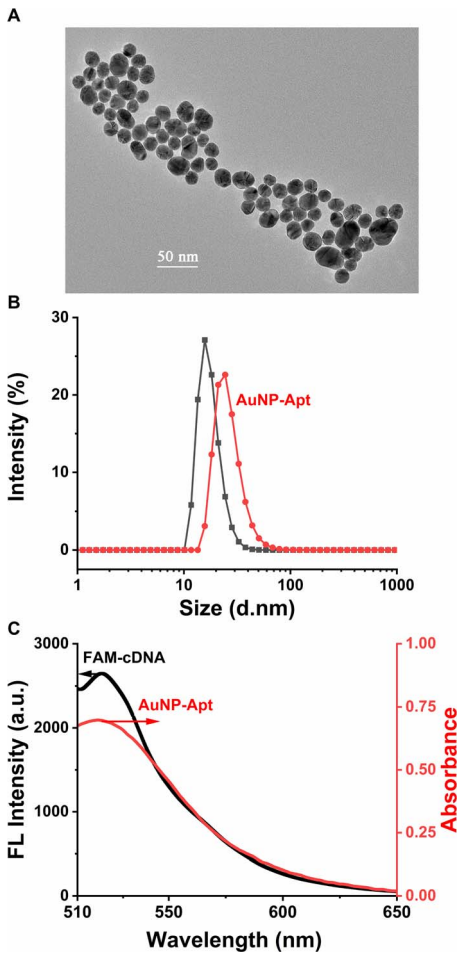

Fig. 2 (A) TEM image of the as-prepared AuNPs. (B) Hydrodynamic diameter distribution of the AuNPs before and after DNA conjugation. (C) Emission of the FAM-cDNA and absorption of the as-prepared AuNP-Apt.

shown in Fig. S1, the AuNPs functionalized with aptamers *via* the freezing method effectively retained their characteristic absorption peak at 520 nm, and the solution color remained pink, identical to that of bare AuNPs. In contrast, the AuNPs frozen without aptamers lost this absorption peak and exhibited a color change to purple. These results demonstrate that PFOA aptamers can effectively protect AuNPs during the freezing process. Upon modification with the aptamer, the UV-vis spectrum shows a distinct enhancement of the absorption peak at 260 nm (Fig. S1), characteristic of nucleic acid bases, confirming successful binding of DNA to the AuNP surface. Consistent with this, the hydrodynamic diameter of the AuNPs increases after aptamer modification (Fig. 2B), further verifying the attachment of aptamers. Moreover, in Fig. 2C, the characteristic absorption peak at 520 nm of AuNPs overlaps strongly with the emission maximum (at ~518 nm) of the FAM fluorescent dye. This spectral overlap provides favorable conditions for constructing a FRET-based sensing platform. The donor–acceptor distance in the hybridized probe was estimated geometrically. The polyA tail adopts a flat conformation on the AuNP surface (~0.5 nm), and the 13-bp duplex formed upon hybridization of FAM-cDNA with the aptamer extends the FAM label a further ~4.42 nm (13 bp × 0.34 nm bp^{-1}), giving an estimated FAM-to-AuNP surface distance of ~4.9 nm. The Förster radius (R_0) was calculated as 25.3 nm (see the SI, page S7). Since the estimated donor–acceptor distance (~4.9 nm) is far below R_0, the classical Förster model predicts near-complete energy transfer, consistent with the high quenching efficiency observed experimentally.

The optimization of AuNP-Apt concentration for the hybridization with FAM-cDNA was first examined. With the concentration of FAM-cDNA fixed at 60 nmol L^{-1}, the fluorescence intensity of FAM gradually decreased as the AuNP-Apt

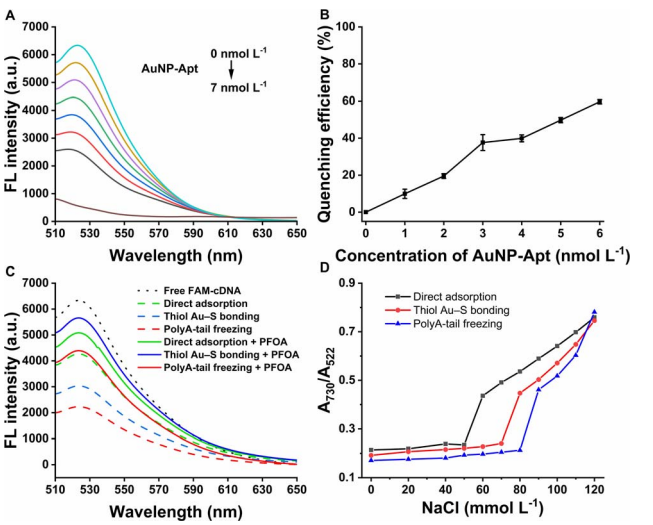

Fig. 3 (A) Effect of AuNP-Apt concentration on the FL intensity of FAM-cDNA. (B) Quenching efficiency ($\Delta F/F_0$) with increase of AuNP-Apt concentration (error bars indicate the standard deviation from three independent measurements). (C) Fluorescence spectra of FAM-cDNA (60 nmol L^{-1}) showing quenching (dashed lines) and recovery upon addition of 100 nmol L^{-1} PFOA (solid lines) for thiol Au–S bonding, direct adsorption and polyA-tail freezing immobilization strategies. Free FAM-cDNA (dotted line) is shown as reference. (D) Colloidal stability of AuNP-Apt conjugates prepared by three immobilization strategies, assessed by the absorbance ratio A_{730}/A_{522} as a function of NaCl concentration.

Table 1 Comparison of three aptamer immobilization strategies on AuNPs

Parameter	PolyA-tail freezing	Thiol Au–S bonding	Direct adsorption
Quenching efficiency (%) ($\Delta F/F_0$)	59.7	52.2	33.3
Fluorescence recovery (+100 nmol L^{-1} PFOA)	2150	2090	1165
Salt tolerance (mmol L^{-1} NaCl)	80	70	50
Preparation time	~3 h	>24 h	~3 h

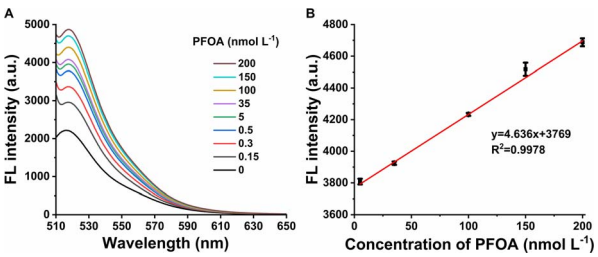

Fig. 4 (A) Fluorescence intensity of the aptasensor upon addition of different concentrations of PFOA. (B) Plot of the fluorescence intensity as a function of PFOA concentration (error bars indicate the standard deviation from three independent measurements).

concentration increased, accompanied by a rise in quenching efficiency (Fig. 3A). The highest quenching efficiency (~59.7%) was achieved at an AuNP-Apt concentration of 6 nmol L^{-1} (Fig. 3B). When the concentration increased to 7 nmol L^{-1}, the characteristic absorption peak of AuNPs at 520 nm disappeared, indicating potential nanoparticle instability or aggregation. Therefore, 6 nmol L^{-1} was selected as the optimal working concentration for subsequent experiments.

To confirm that the fluorescence quenching originated from specific DNA hybridization rather than nonspecific adsorption, control experiments were carried out by incubating FAM-cDNA (60 nmol L^{-1}) with bare AuNPs (6 nmol L^{-1}) and with AuNP-Apt (6 nmol L^{-1}), respectively (Fig. S2). While no significant fluorescence change was observed in the presence of bare AuNPs, a pronounced decrease occurred with AuNP-Apt. This result verifies that the quenching is due to FRET between FAM and AuNPs brought into close proximity through hybridization, thereby demonstrating the specificity of the AuNP-Apt probe.

Comparative experiments using three immobilization strategies — polyA-tail-mediated freezing, thiol-based Au–S bonding, and direct adsorption — revealed marked differences in sensing performance (Table 1, Fig. 3C and D). The polyA-tail approach achieved the highest quenching efficiency (59.7%), outperforming thiol-based bonding (52.2%) and direct adsorption (33.3%), which can be attributed to the flat-lying polyA tail positioning the aptamer sequence in a well-oriented, upright conformation that facilitates efficient FAM-to-AuNP energy transfer. Upon PFOA addition, the polyA-tail conjugates also yielded the greatest fluorescence recovery (2150 a.u. *vs.* 2090 and 1165 a.u., respectively), reflecting more complete competitive displacement of FAM-cDNA. Furthermore, the polyA-tail strategy demonstrated superior salt tolerance (80 mmol L^{-1} NaCl), likely because the densely packed polyA layer provides electrostatic shielding that stabilizes the AuNP surface against aggregation (Fig. 3D). The preparation process of the thiol-based (Au–S) bonding method required over 24 h, which is somewhat disadvantageous compared to the ~3 h needed for the polyA-tail freezing method. Taken together, the polyA-tail freezing approach was therefore adopted as the preferred immobilization strategy in this work.

Under the optimized conditions, the analytical performance of the method was evaluated by measuring a series of PFOA standard solutions. As depicted in Fig. 4A, in the absence of PFOA, the fluorescence of FAM-cDNA was efficiently quenched by AuNP-Apt, yielding the lowest fluorescence signal. Upon addition of PFOA, the fluorescence intensity gradually increased due to the competitive displacement of FAM-cDNA from the AuNP-Apt complex. The fluorescence intensity (F) showed a good linear relationship with PFOA concentration in the range of 5 nmol L^{-1} to 200 nmol L^{-1}, with a regression equation of $F = 4.636\ C_{(PFOA)} + 3769$ ($R^2 = 0.9978$), and a detection limit (3σ) of 1.3 nmol L^{-1} (Fig. 4B).

A comparison with previously reported methods (Tables S2 and S3) shows that the detection limit of the proposed aptasensor is lower than that of most fluorescence-based approaches. While LC-MS/MS remains superior in sensitivity and multi-analyte capability, the proposed method requires only a fluorescence spectrometer for detection, avoiding the need for expensive chromatography-mass spectrometry instrumentation.

The instrument precision was evaluated by 11 consecutive measurements of 100 nmol L^{-1} PFOA, yielding an RSD of 1.1%. The method precision and accuracy were further evaluated

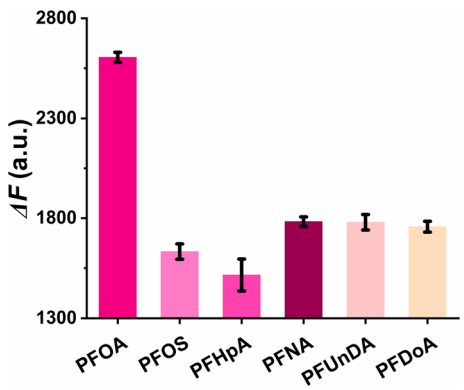

Fig. 5 Specificity of the aptasensor assessed by its response to PFOA (400 nmol L^{-1}) *versus* other PFASs (PFOS, PFHpA, PFNA, PFUnDA, and PFDoA at 50–100 μmol L^{-1}).

Table 2 Analytical results for the proposed aptasensor for the determination of PFOA in fish samples[a]

Sample	Spiked PFOA (nmol L^{-1})	Concentration determined (mean ± s, $n = 3$) (nmol L^{-1})	Recovery (%) (mean ± s, $n = 3$)
Crucian carp	0	ND	—
	5	4.83 ± 0.62	96.6 ± 12.4
	50	51.95 ± 2.35	103.9 ± 4.9
	100	96.80 ± 13.22	96.8 ± 13.2
Perch 1	0	ND	—
	5	4.62 ± 0.32	92.4 ± 6.3
	50	47.85 ± 7.05	95.7 ± 4.1
	100	89.90 ± 3.86	89.9 ± 3.8
Perch 2	0	ND	—
	5	4.95 ± 0.48	99.0 ± 9.6
	50	49.10 ± 1.45	98.2 ± 2.9
	100	100.70 ± 11.40	100.7 ± 11.4

[a] ND: not detected.

using quality control (QC) samples at three concentration levels (100, 150, and 200 nmol L^{-1}). Intra-batch RSDs ranged from 5.7% to 8.4% ($n = 6$), and inter-batch RSDs ranged from 9.0% to 11.8%. The inaccuracy at all quality control concentration levels was within ±15%, confirming acceptable method performance (Fig. S3 and Table S4).

The specificity of the assay was investigated by challenging it with various structurally related per- and polyfluoroalkyl substances (PFASs) commonly found in food samples, including PFOS, PFHpA, PFNA, PFUnDA and PFDoA. As shown in Fig. 5, a significant fluorescence recovery was observed only in the presence of PFOA, while the other PFASs exhibited negligible signal changes. This demonstrates the high binding specificity of the employed aptamer toward PFOA. The sensing platform exhibits excellent selectivity for PFOA against its common analogues, which is crucial for reliable analysis in complex matrices.

To validate the feasibility and accuracy of the developed aptasensor, PFOA was detected in crucian carp and perch using a standard addition (spike-and-recovery) approach. The samples were spiked with PFOA at concentrations of 5, 50, and 100 nmol L^{-1}. As shown in Table 2, the application to spiked fish samples yielded recoveries of 89.9–103.9%, indicating acceptable matrix tolerance. It should be noted that PFOA was not detected in any unspiked fish samples, which is consistent with the generally low contamination levels reported in fish tissue. Future work should include the analysis of naturally contaminated samples and cross-validation against LC-MS/MS to further establish the method accuracy.

Conclusions

A sensitive and selective FRET-based aptasensor has been successfully developed for the detection of PFOA. The sensing platform relies on the competitive displacement of a FAM-labeled cDNA strand from gold nanoparticle-bound PFOA aptamers, resulting in measurable fluorescence recovery. Under optimized conditions, the assay exhibits a wide dynamic range from the nanomolar to hundreds of nanomolar concentrations, achieving a low detection limit of 1.3 nmol L^{-1}. Excellent specificity toward PFOA over other common PFAS analogues was demonstrated, which originates from the high-affinity recognition of the employed aptamer. Application to spiked fish samples yielded recoveries of 89.9–103.9%, indicating acceptable matrix tolerance. These results indicate that the proposed strategy offers a rapid and practical approach for screening PFOA contamination in food matrices. Looking forward, the modular design of this sensing platform offers considerable flexibility for broader applications. By substituting the aptamer sequence, the same AuNP-based FRET strategy could be readily adapted for the detection of other PFASs or emerging environmental contaminants. Integration with portable fluorescence readers would further enable point-of-use field screening, which is particularly desirable for rapid on-site monitoring in food safety and environmental surveillance.

Author contributions

Zhuo-Ying Li: investigation, data curation, writing – original draft. Li-Xia Yan: methodology, funding acquisition. Xu Zhao: investigation, methodology. Li-Jian Chen: methodology, supervision, writing – review & editing. Xiu-Ping Yan: conceptualization, writing – review & editing.

Conflicts of interest

There are no conflicts to declare.

Data availability

The data supporting this article have been included as part of the supplementary information (SI). Supplementary information: UV-vis absorption spectra of AuNPs with different treatments, fluorescence spectra of FAM-cDNA with bare AuNPs/AuNP-Apt, intra-batch and inter-batch reproducibility

evaluation, respectively, Tables S1–S4, and further experimental details. See DOI: https://doi.org/10.1039/d6ay00236f.

Acknowledgements

This work was supported by the National Natural Science Foundation of China (22304063) and the Natural Science Foundation of Jiangsu Province, China (No. BK20231033).

Notes and references

1 E. Panieri, K. Baralic, D. Djukic-Cosic, A. Buha Djordjevic and L. Saso, *Toxics*, 2022, **10**, 44.
2 M. G. Evich, M. J. B. Davis, J. P. McCord, B. Acrey, J. A. Awkerman, D. R. U. Knappe, A. B. Lindstrom, T. F. Speth, C. Tebes-Stevens, M. J. Strynar, Z. Wang, E. J. Weber, W. M. Henderson and J. W. Washington, *Science*, 2022, **375**, eabg9065.
3 V. Marra, A. Abballe, E. Dellatte, N. Iacovella, A. M. Ingelido and E. De Felip, *Int. J. Anal. Chem.*, 2020, 8878618.
4 G. Lv, L. Wang, S. Liu and S. Li, *Anal. Sci.*, 2009, **25**, 425–429.
5 I. Zabaleta, E. Bizkarguenaga, A. Prieto, M. Ortiz-Zarragoitia, L. A. Fernandez and O. Zuloaga, *J. Chromatogr., A*, 2015, **1387**, 13–23.
6 D. Zacs, D. Fedorenko, E. Pasecnaja and V. Bartkevics, *Anal. Chim. Acta*, 2023, **1251**, 341027.
7 M. Dalapati, M. Sk. Hunter, X. Yang and L. Zang, *ACS Appl. Mater. Interfaces*, 2024, **16**, 32344–32356.
8 J. Su, Q. Niu, J. Liu, X. Liu, Y. Wang, Z. Ge, Y. Ye and Z. Li, *Chem. Eng. J.*, 2025, **520**, 166124.
9 N. Yang, X. Lin, X. Zheng, W. Lai, Y. Lin, Z. Zou, Q. Wang and X. Zheng, *Microchim. Acta*, 2025, **192**, 134.
10 R. Dalapati, J. Shi, M. Hunter and L. Zang, *J. Mater. Chem. C*, 2025, **13**, 16753–16762.
11 S. Chen, A. Li, L. Zhang and J. Gong, *Anal. Chim. Acta*, 2015, **896**, 68–77.
12 Y. Guo, Z. Li, W. Li, X. Chen and Z. Cai, *Talanta*, 2025, **294**, 128244.
13 C. Fang, Z. Chen, M. Megharaj and R. Naidu, *Environ. Technol. Innov.*, 2016, **5**, 52–59.
14 Y. Han, D. Diao, Z. Lu, X. Li, Q. Guo, Y. Huo, Q. Xu, Y. Li, S. Cao, J. Wang, Y. Wang, J. Zhao, Z. Li, M. He, Z. Luo and X. Lou, *Anal. Chem.*, 2017, **89**, 5270–5277.
15 B. Wang, B. Park, B. Xu and Y. Kwon, *J. Nanobiotechnol.*, 2017, **15**, 40.
16 M. S. Song, S. S. Sekhon, W. R. Shin, H. C. Kim, J. Min, J. Y. Ahn and Y. H. Kim, *Molecules*, 2017, **22**, 825.
17 L. Hu, L. Wang, W. Lu, J. Zhao, H. Zhang and W. Chen, *Int. J. Mol. Sci.*, 2017, **18**, 833.
18 W. Zhao, W. Chiuman, J. C. Lam, S. A. McManus, W. Chen, Y. Cui, R. Pelton, M. A. Brook and Y. Li, *J. Am. Chem. Soc.*, 2008, **130**, 3610–3618.
19 P. Li, C. Luo, X. Chen and C. Huang, *RSC Adv.*, 2022, **12**, 35763–35769.
20 Y. Liu, Q. Ouyang, H. Li, M. Chen, Z. Zhang and Q. Chen, *J. Agric. Food Chem.*, 2018, **66**, 6188–6195.
21 M. Cardenas, J. Barauskas, K. Schillen, J. L. Brennan, M. Brust and T. Nylander, *Langmuir*, 2006, **22**, 3294–3299.
22 A. G. Kanaras, Z. Wang, A. D. Bates, R. Cosstick and M. Brust, *Angew. Chem., Int. Ed.*, 2003, **42**, 191–194.
23 B. Liu, P. Wu, Z. Huang, L. Ma and J. Liu, *J. Am. Chem. Soc.*, 2018, **140**, 4499–4502.
24 X. Zhang, M. R. Servos and J. Liu, *J. Am. Chem. Soc.*, 2012, **134**, 7266–7269.
25 B. Liu and J. Liu, *J. Am. Chem. Soc.*, 2017, **139**, 9471–9474.
26 H. Pei, F. Li, Y. Wan, M. Wei, H. Liu, Y. Su, N. Chen, Q. Huang and C. Fan, *J. Am. Chem. Soc.*, 2012, **134**, 11876–11879.
27 M. Hu, C. Yuan, T. Tian, X. Wang, J. Sun, E. Xiong and X. Zhou, *J. Am. Chem. Soc.*, 2020, **142**, 7506–7513.
28 X. Hua, J. Fan, L. Yang, J. Wang, Y. Wen, L. Su and X. Zhang, *Biosens. Bioelectron.*, 2022, **198**, 113830.
29 S. M. Schreiner, D. F. Shudy, A. L. Hatch, A. Opdahl, L. J. Whitman and D. Y. Petrovykh, *Anal. Chem.*, 2010, **82**, 2803–2810.
30 J. Park, K. A. Yang, Y. Choi and J. K. Choe, *Environ. Int.*, 2022, **158**, 107000.

